J Mater Sci (2024) 59:1348–1363

Composites & nanocomposites

Broadband electrical conductivity of metal/carbon nanotubes polyamide 6 composites fabricated by reactive encapsulation

Filipa M. Oliveira[1,3], Tiberio A. Ezquerra[2], and Zlatan Z. Denchev[1,*]

[1] *Institute for Polymers and Composites, University of Minho, 4800-058 Guimarães, Portugal*
[2] *Instituto de Estructura de la Materia, IEM-CSIC, Serrano 121, 28006 Madrid, Spain*
[3] *Present Address: Department of Inorganic Chemistry, University of Chemistry and Technology Prague, Technická 5, 166 28 Prague 6, Czech Republic*

Received: 17 August 2023
Accepted: 16 December 2023
Published online: 14 January 2024

ABSTRACT

This is the first broadband dielectric spectroscopy study on the temperature- and frequency-dependent electrical conductivity of polyamide 6 (PA6) composites containing both metal microparticles (Al, Fe, or Cu) and carbon nanotubes (CNT). The dually reinforced PA6 hybrids are prepared through compression molding of metal- and CNT-loaded microparticles (MP). These MP are synthesized by activated anionic ring-opening polymerization (AAROP) of ε-caprolactam in suspension, carried out in the presence of the micron-sized metal powders and the nanosized CNT fillers, with a combined load of up to 10 wt%. The good dispersion of the two loads by the AAROP strategy results in a notable increase in the electrical conductivity by up to 11 orders of magnitude. Moreover, the frequency-dependent behavior of the measured conductivity obeys the so-called universal dynamic response. This response involves a direct current (d.c.) electrical conductivity (σ_{dc}) observed beyond a critical frequency, F_c, followed by a power-law response characterized by an exponent s, which fluctuates between 0.11 and 0.43. The σ_{dc} of the binary composites spans from 1.42×10^{-5} to 1.63×10^{-2} S/cm, this increase being attributed to the synergetic effect between CNT and the metal particles that contribute to the carrier mobility within the conductive network.

Handling Editor: Maude Jimenez.

Address correspondence to E-mail: denchev@dep.uminho.pt

https://doi.org/10.1007/s10853-023-09288-4

GRAPHICAL ABSTRACT

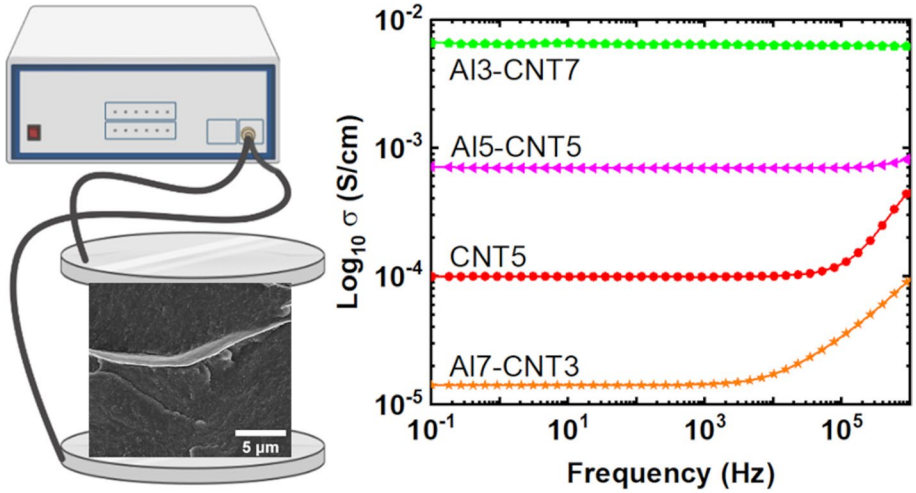

Introduction

Polyamide 6 (PA6) stands as one of the most widely utilized thermoplastics, owing to the accessibility of its monomer, ε-caprolactam (ECL), its adaptability across a broad spectrum of applications, and the economic viability of its production, processing, and recycling. PA6 combines properties such as high strength and toughness, effective resistance to chemicals and abrasion, and considerable thermal stability. These characteristics position PA6 as the primary choice for the manufacture of thermoplastic materials. PA6 finds application in a diverse range of industries, spanning automotive components, industrial parts, construction materials, electronic devices, and textile structures, among others [1, 2].

As an insulating material, PA6 has been the subject of investigation using dielectric spectroscopy [3–12], alongside with other polyamides and their blends [13–18]. The dielectric behavior of polyamides is closely related to their semi-crystalline nature and the strong interchain interactions by hydrogen bonding between amide groups. Polyamides are polar and tend to absorb water leading to a decrease in the glass transition temperature and changes in local mobility [5, 6]. In general, the dielectric spectra of polyamides reveal three main mechanisms associated with molecular motions. These involve two local motions, referred to as the γ- and β-relaxations, which are predominant at lower temperatures, and the segmental α-relaxation at higher temperatures, the latter being related to the glass transition of the amorphous phase. Furthermore, at temperatures above the α-transition, an interfacial polarization phenomenon known as Maxwell–Wagner–Sillars (MWS) polarization becomes observable. This polarization emerges from the trapping of free charges at the boundaries between crystalline and amorphous regions [14, 15]. It is worth noting that conductivity effects in polyamides have only been found to be significant at relatively high temperatures [7].

To control or modify the insulating characteristics of polymers, conductive fillers have been employed. These fillers enable the formation of a continuous conductive network within the polymer matrix. Various examples of such fillers include different carbon allotropes [19–23], metal particles [24–26], or intrinsically conducting polymers [27, 28]. Carbon nanotubes (CNT) are among the most extensively researched conductive carbon fillers employed in polymer composites due to their ability to significantly enhance electrical conductivity even in small quantities [29–33]. However, CNT have a substantial cost and tend to agglomerate during the traditional melt processing of composites that contain them. Consequently, researchers have also explored the electric and dielectric response of polymer composites containing alternative carbon-based conductive fillers, including graphite [34], carbon black [3], carbon nanofibers [35], graphene [36], and fullerene derivatives [37].

The utilization of metal micro- and nanoparticles to fine-tune the electrical conductivity of polymer matrices has been less common. This is primarily due to their high density, limited corrosion resistance, and the associated high processing costs [38, 39]. Instead, there is a growing trend of combining carbon and metal fillers. For instance, this is achieved by coating carbon fibers with metals using cementation and electroless deposition techniques, with copper (Cu) or nickel (Ni) being the most commonly used metals [40]. However, it should be noted that these techniques are relatively complex and costly, especially for large-scale industrial applications.

One possible approach to prepare polymer composites with various fillers that have distinct electrical, dielectric, and magnetic properties is the use of core–shell micro- and nanoarchitecture strategies [41]. In this method, each micro- or nanosized filler particle is encapsulated by the matrix polymer using different polymerization techniques. The resulting microparticles can then be transformed into polymer composites through conventional molding techniques. A similar two-stage synthetic process has been effectively employed to produce PA6 hybrids containing both metal and carbonaceous fillers [42, 43]. First, activated anionic ring-opening polymerization (AAROP) of ECL is performed in a hydrocarbon suspension containing metal [42–44], carbon allotropes [43, 45], or their mixture [46]. This leads to the production of PA6 microparticles (PA-MP) loaded with the fillers. Then, the PA-MP are molded into PA6 composite plates using compression molding.

In our previous work [46], we described the synthesis of PA-MP loaded with both metals and CNT using AAROP in their presence and their subsequent conversion into molded composite plates. Our investigation demonstrated that by changing the type and ratio of metal and CNT, we could produce binary PA6-based composites exhibiting a significant increase in electrical conductivity. This enhanced electrical conductivity resulted in a good performance in terms of electromagnetic shielding properties [47]. So far, however, no studies have explored the frequency- and temperature-dependent conductivity of these dually loaded composites obtained via AAROP. Broadband dielectric spectroscopy (BDS), a technique that reflects both molecular relaxation and electrical conductivity phenomena [48], has proven to be an effective non-destructive method for the electrical characterization of polymer composites over a wide frequency range.

This study is the first report on the frequency and temperature dependence of the electrical conductivity in PA6-based composites loaded with both metal and CNT (Me-CNT) fillers, obtained through reactive encapsulation followed by compression molding. Cu, Al, and Fe are all abundant and industrially important metals that can be pulverized into micron-sized particles relatively easily. Notably, the nature of the metal directly influences the shape and size of the resulting particles. Moreover, Al and Cu are excellent electrical conductors with diamagnetic or paramagnetic properties, respectively, whereas Fe has lower electrical conductivity but displays ferromagnetic properties. Al is a lightweight metal with a density of 2.7 g/cm^3, while Cu and Fe are considerably denser, with densities of 8.99 g/cm^3 and 7.87 g/cm^3, respectively.

The electrical conductivity of various dually loaded PA6 composites is determined over a wide range of frequencies and temperatures, i.e., $-150 \le T\,(^\circ\mathrm{C}) \le 100$ and $10^{-1} < f\,(\mathrm{Hz}) < 10^6$. This BDS study reveals the synergy between the metal and CNT fillers that enhance the electrical conductivity of metal/carbon PA6 composites. It contributes to a deeper comprehension of the nature of electrical conductivity in polymer composites loaded with mixed Me-CNT fillers that could lead to novel effective applications.

Experimental section

Materials

The ECL monomer, AP-Nylon® Caprolactam, with reduced moisture content, was purchased from Brüggemann Chemical, Germany. Difunctional hexamethylene-1,6-dicarbamoyl-caprolactam, Bruggolen C20P® (C20), purchased from Brüggemann Chemical, Germany, was used as a polymerization activator. According to the manufacturer, it contains 17 wt% of di-isocyanate blocked in ECL. Sodium dicaprolactamo-bis-(2-methoxyethoxo)-aluminate, Dilactamate® (DL), 80% in toluene solution, delivered by Katchem Co., Czech Republic, was used as the polymerization initiator. The powders of Cu (> 99.5%, grain size < 40 μm) and Al (> 93%, grain size < 100 μm) were supplied by Merck–Sigma-Aldrich. The soft, non-insulated carbonyl Fe powder (> 99.5, average grain size 3–5 μm) was kindly donated by the BASF Group, Germany. The multi-walled CNT (MWCNT, ≥ 98% carbon basis) with an outer diameter of 10 nm and length of 3–6 μm

were purchased from Merck-Sigma-Aldrich. Toluene, methanol, and other solvents, all of "puriss" grade, were purchased from Sigma-Aldrich. All chemical reagents, payloads, and solvents were used as received, without further treatment.

Preparation of the microparticles and respective composites

The synthesis of the loaded PA-MP involved the solution-precipitation AAROP of ECL, following a procedure published elsewhere [43, 46]. In a typical polymerization process for neat PA-MP, 0.5 mol of ECL were introduced into a toluene/xylene mixture (180 mL) under stirring. The mixture was then refluxed under a N_2 atmosphere for 10–15 min to stabilize it. Subsequently, 3 mol% of DL and 1.5 mol% of C20 were added at once. The polymerization was carried out for 2 h while maintaining the temperature in the range of 125–135 °C at a constant stirring rate of ca. 800 rpm. The neat PA-MP were obtained in the form of fine white powder and separated from the reaction mixture through hot vacuum filtration. They were then washed several times with methanol and dried for 4 h at 80 °C in a vacuum oven.

For the mono-loaded PA and dually loaded PA-MP, a mixture containing the desired quantities of CNT, metal particles (Al, Cu, or Fe), or a combination of both was introduced into the polymerization medium. In the case of samples containing CNT, a sonication process was conducted for 30 min as a part of the protocol to prevent agglomeration. The mixture was then added to the ECL, and the total solvent volume was adjusted to 180 mL. From this point onward, the AAROP procedure was executed as it was for the neat PA-MP. The mono- and metal-CNT-loaded PA-MP were obtained as a fine dark powder with metallic luster typical of the respective load and were isolated from the reaction mixture, washed, and dried in the same way as for neat empty PA-MP.

The compression molding of the PA-MP into composite plates was carried out in a 25-ton Moore hydraulic hot press (England). A rectangular mold with dimensions of 85 × 75 × 1 mm was employed. The quantity of each PA-MP deposited into the mold was determined considering the mold's volume, the density of PA6, and the chosen fillers. A pressure of 5 MPa was applied for 5–7 min at 230 °C. Subsequently, the composite plates were cooled down to 80 °C at a rate of 40 °C/min.

Morphological and thermal characterization

Thermogravimetric analysis (TGA) was used to determine the effective real load (R_L) in PA-MP. A Q500 TGA equipment (TA Instruments, USA) was employed, heating the samples from 40 to 600 °C at 10 °C/min in a nitrogen (N_2) atmosphere. The typical sample weights were in the 10–120-mg range. The R_L value was calculated according to Eq. 1:

$$R_L = R_f - R_{PA6}, \% \tag{1}$$

where R_{PA6} is the carbonized residue at 600 °C of empty PA-MP, and R_f represents the carbonized residue of the respective loaded PA-MP measured by TGA.

Differential scanning calorimetry (DSC) measurements were carried out in a 200 F3 equipment of Netzsch (Germany) at a heating rate of 10 °C/min under N_2 purge in the 0–250 °C range. The typical sample weights were in the 10–15-mg range. The crystallinity index, X_c, of the PA6 matrix, was calculated according to Eq. 2:

$$X_c = \frac{\Delta H_m^i}{w \bullet \Delta H_m^0}, \% \tag{2}$$

where ΔH_m^i is the registered melting enthalpy of the current sample, w is the weight fraction of the polymer present in the sample, and ΔH_m^0 is the melting enthalpy of a 100% crystalline PA6 (190 J/g) [49].

Scanning electron microscopy (SEM) analyses were performed in a NanoSEM-200 apparatus of FEI Nova (Hillsboro, USA) using mixed secondary electron/back-scattered electron in-lens detection. The composite samples were cryo-fractured, and the obtained sections were sputter-coated with gold–palladium (Au–Pd) alloy, 80–20 wt%, with a thickness of about 8 nm using a 208 HR equipment of Cressington Scientific Instruments (Watford, UK) with high-resolution thickness control.

Broadband dielectric spectroscopy

To obtain a detailed profile of the temperature- and frequency-dependent electrical properties, the BDS measurements were performed with the composite plates based on dielectric relaxation defined by the complex function [48]:

$$\varepsilon^* = \varepsilon' - i\varepsilon'' \quad (3)$$

where ε^* is the complex dielectric permittivity, ε' is the real component or dielectric constant, and ε'' is the imaginary component or dielectric loss. Thus, sputtered gold electrodes (20 mm in diameter) were deposited on both surfaces of each sample, and the latter was then placed between the two metallic electrodes of the spectrometer. The BDS measurements were performed over a frequency window of $10^{-1} < f\,(\mathrm{Hz}) < 10^6$ and a temperature range of $-150 < T\,(^\circ\mathrm{C}) < 100$. To cover the said frequency range, a Novocontrol system integrating an ALPHA dielectric interface was employed. The control of the temperature during every single-frequency sweep was secured by the N_2 gas jet system (QUATRO Cryosystem from Novocontrol) with a temperature error of ± 0.1 °C. After that, the alternating current (a.c.) electrical conductivity, σ_{ac}, was obtained from the frequency dependence of the real part of ε according to Eq. 4:

$$\sigma_{ac} = \varepsilon'' \bullet \omega \bullet \varepsilon_0 \quad (4)$$

where ω is the angular frequency ($\omega = 2\pi f$), and ε_0 is the vacuum dielectric constant.

Results and discussion

Structural and morphological characterization

All mono- and dually loaded pulverulent PA6 hybrid precursors were prepared through consecutive AAROP of ECL in suspension followed by compression molding to plates. The synthesis, morphology, and crystalline structure of the MP precursors and plates containing metal monoloads and Me-CNT are described in the previous works [46, 47]. This study focuses on the alterations in the electrical conductivity of PA6/metal-CNT composites' response to changes in frequency and temperature, which has not been investigated before. Table 1 summarizes the sample designations and compositions, as well as AAROP yields and real load in each composite.

As shown from Table 1, the sample designation corresponds to the load percentage introduced during the AAROP stage, which is based on the monomer weight (column 2). The real load (R_L) is consistently higher since no load is lost during the isolation of the MP, resulting in a yield of PA6 MP always below 100%. Notably, only this strategy, including microencapsulation of the two loads in PA6 MP with their subsequent compression molding into plates, ensures an effective distribution of the Me-CNT binary load throughout the PA6 matrix [46]. In the monoload MP, the real

Table 1 Sample designations, compositions, yields, and percentages of load

Sample designation	Load (wt%)[a]	Composition (vol.%)[b]			Yield (wt%)[c]	Real load (wt%)[d]
		Metal	CNT	PA6		
PA6	0	0	0	100	56.2	–
CNT5	5	0	4.45	95.6	53.2	8.2
Al5	5	4.18	0	95.8	45.9	9.4
Cu5	5	1.33	0	98.7	42.4	9.6
Fe5	5	1.06	0	98.9	45.3	7.0
Al3-CNT7	3 + 7	1.96	5.71	92.3	61.0	14.4
Al5-CNT5	5 + 5	3.84	4.80	91.4	56.4	16.7
Al7-CNT3	7 + 3	4.68	2.51	92.8	58.9	14.7
Cu5-CNT5	5 + 5	1.03	4.29	94.7	51.8	14.8
Fe5-CNT5	5 + 5	0.93	3.38	95.7	63.0	11.9

[a]Percentage based on the weight of the ECL monomer in the starting AAROP mixture

[b]The relation between the volumes of load (metal-CNT or metal + CNT) and PA6 in the respective PA6-MP sample

[c]Calculated as a relation between the PA6-MP weight and the sum of the ECL plus fillers weight

[d]Determined by TGA according to Eq. 1

amount of the CNT is ca. 8 wt%, i.e., well above the percolation threshold in PA6 [50]. The metal load in both mono- and dually loaded samples in Table 1 varies between 1 and 5 vol.%. These metal and CNT loads are close to the maximal since any attempt to increase either of them during AAROP results in significantly lower yields of the MP precursors.

Figure 1 shows the SEM images of selected cryo-fractured molded plates produced from the respective PA-MP. In the monoload metal composites (Fig. 1a–c), the electron-rich metal particles are observed as microsized and differently shaped bright spots, fully enclosed in the non-conductive, dark PA6 matrix. In the Me-CNT binary loaded samples (Fig. 1d–f), the CNT filler particles are visible as bright nanospots, well-dispersed throughout the polymer. Furthermore, there is visible good contact between the CNT and metal particles, which is most clearly observed in Fig. 1f.

Based on the SEM data presented in Fig. 1, the microstructure of the monoload metal-PA6 (Me-PA6) samples can be likened to a composition of many capacitors where conductive metal domains are separated by relatively large insulating PA6 matrix zones. The SEM micrographs clearly illustrate the distinct presence of white spots that correspond to the metal fillers themselves—Al appears as platelets (Fig. 1a), Cu adopts dendritic-like shapes (Fig. 1b), and Fe presents spherical particles (Fig. 1c) [47]. It is important to note that the metal fillers maintain their morphology after compression molding.

In contrast, the microstructure of dually loaded Me-CNT samples, as shown in Fig. 1d-f, closely corresponds to a network of randomly connected resistors. Conductive zones are formed by the contact between metal and CNT while insulating zones are represented by PA6 with either no or insufficient CNT nanofiller. This structural description aligns with findings in the works of Almond et al. [51–53] and is commonly referred to as a random R–C network.

Notably, these SEM images reveal fewer white spots and a distinct absence of filler aggregation in the composite plates of dually loaded Me-CNT. The small, bright nanometric dots observed in these images correspond to the CNT, highlighting their effective spreading within the PA6 matrix. Furthermore, CNT dispersion extends atop the metal particles, creating an even distribution. Consequently, the metal particles

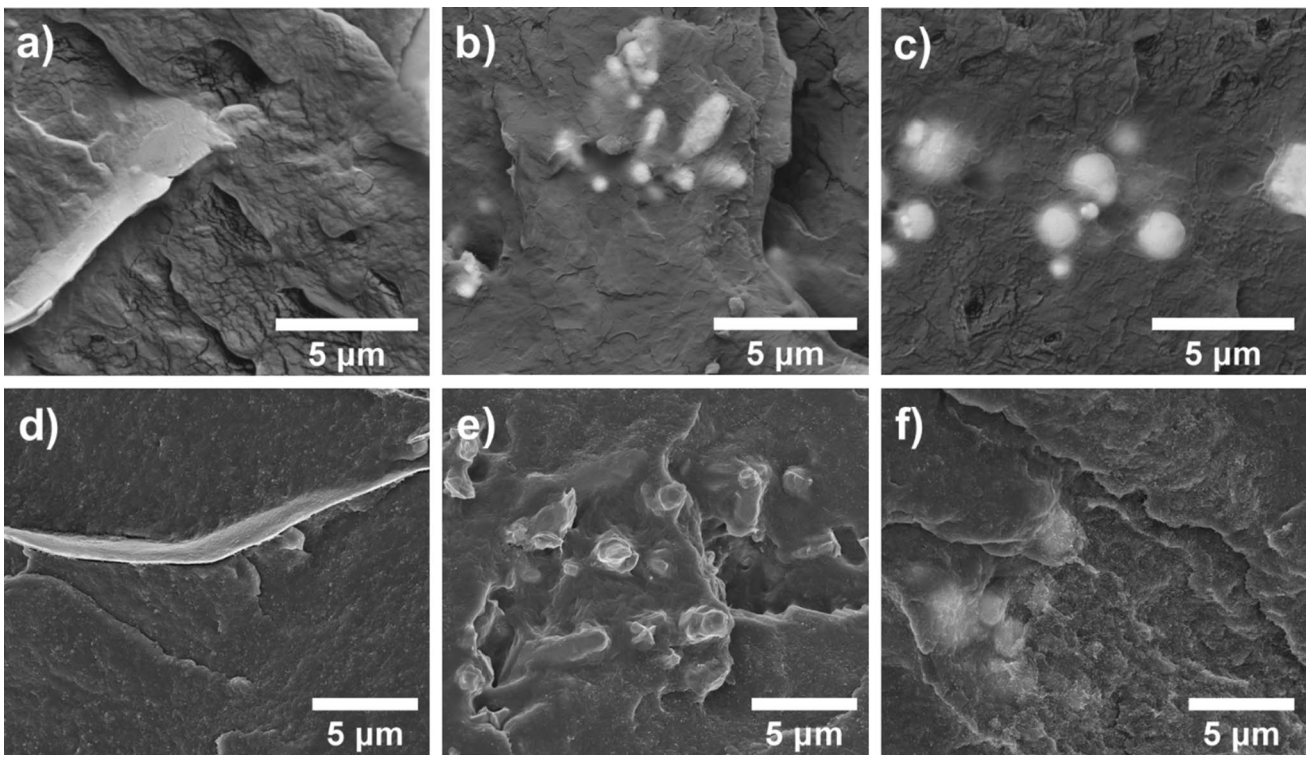

Figure 1 SEM micrographs of composite plates containing metal (5 wt%) and metal/CNT (5 + 5 wt%) loads: **a** Al5, **b** Cu5, **c** Fe5, **d** Al5-CNT5, **e** Cu5-CNT5, and **f** Fe5-CNT5.

appear less bright than in the composites with only metal (Fig. 1a–c). This phenomenon can be attributed to several factors, including the high aspect ratio of CNT and their excellent dispersion within the polymer matrix, significantly reducing filler aggregation. This, in turn, promotes the formation of a continuous conducting network within the composite that results in a more effective charge carrier movement. This effect is expected to improve the conductivity in the dually loaded Me-CNT composites.

Comparative DSC studies on PA6 composites

Table S1 of the Supporting information presents the T_m and X_c of all composite plates under investigation after the first DSC scan. The X_c values of almost all samples (except for Cu5) vary in the range of 34–46%, which is clearly above that of the neat PA6 (X_c = 24%). Having in mind that the composite plates were obtained by compression molding of hybrid microparticles, the increased crystallinity of the composite plates should be explained with the strong nucleating effect of the fillers, best expressed in the mono-loaded CNT5 and all dually loaded samples. This is confirmed by the T_c values in Table S1, wherein the neat PA6 displays a T_c being up to 14–17 °C lower than the composites.

During the first DSC scan, the respective T_g transitions were superimposed with physical aging effects so they could not be properly determined and analyzed. This was made using the T_g values of the second scan that were all around 45–50 °C. Notably, after the second scan, the T_m and X_c values of the composite plates become quite similar. More comprehensive DSC and TGA studies, as well as solid-state ^{13}C NMR and mechanical tests in tension with all samples investigated by BDS in this work, have been communicated by us previously [46].

Broadband electrical conductivity of the binary composites

Figure 2 shows the logarithmic plots of the a.c. electrical conductivity, σ_{ac}, versus frequency for the neat PA6 plates (Fig. 2a) and plates produced from mono-loaded PA-MP with 5 wt% of either Al (Fig. 2b) or CNT (Fig. 2c). Notably, for both the neat PA6 (Fig. 2a) and the Al5 hybrid (Fig. 2b), the $\sigma(\omega)$ function exhibits linearity within the frequency range of 10^{-1}–10^{6} Hz at temperatures ranging from − 150 to 0 °C. This range falls below the glass transition temperature, T_g, of the matrix, which

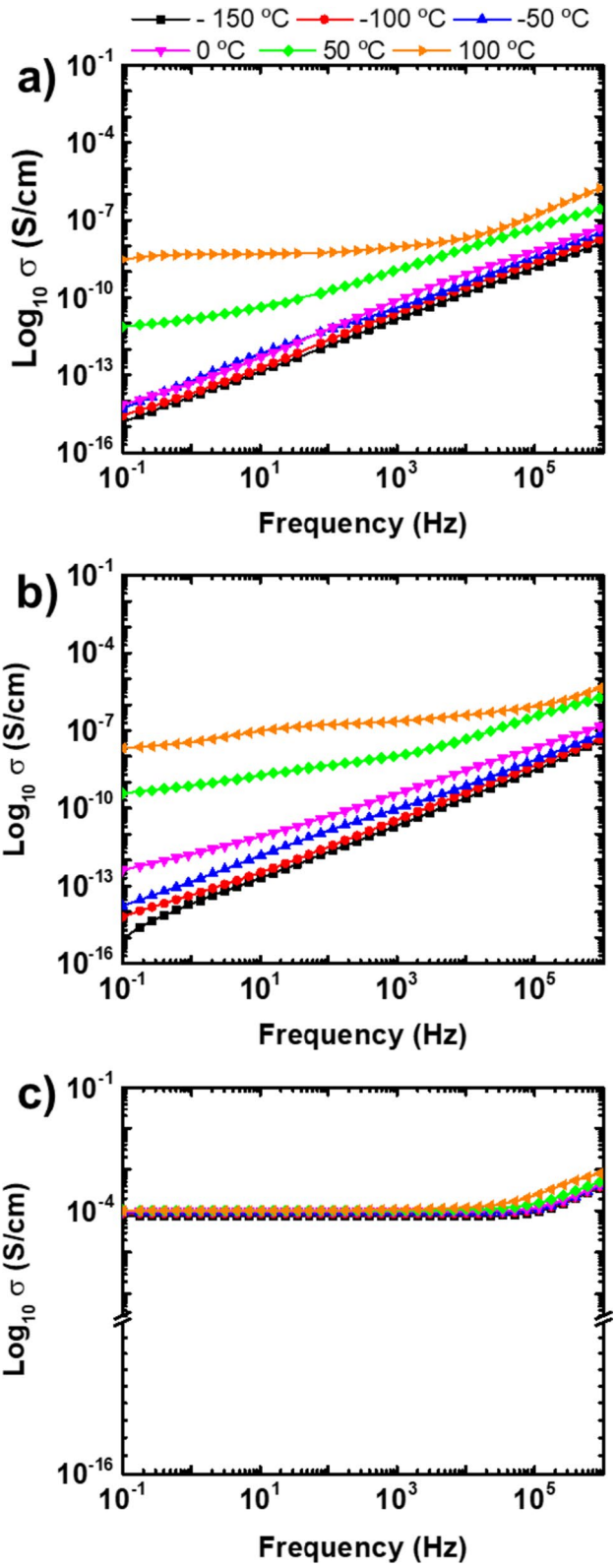

Figure 2 Electrical conductivity σ_{ac} as a function of frequency at different temperatures for **a** PA6, **b** Al5, and **c** CNT5 composite plates.

for all samples of this study is below 50 °C (see Table S1). At temperatures above T_g, $T > T_g$, (i.e., at 50 and 100 °C), the nonlinear behavior of $\sigma(\omega)$ may be attributed to the segmental α-relaxation associated with the glass transition in the amorphous phase of the matrix [54, 55]. Both the PA6 matrix and Al5 hybrid exhibit conductivity values ranging from 10^{-14} to 10^{-12} S/cm at lower frequencies, which converge to 10^{-8} S/cm at higher frequencies. The Cu5 and Fe5 hybrids display very similar frequency dependencies. Table 2 presents the conductivity values at 0.1 Hz for PA6 and Me-PA6 samples as a function of the metal load and type.

From the data presented in Fig. 2a and b and Table 2, it can be inferred that both the PA6 matrix and monoload Me-PA6 composites display relatively similar frequency- and temperature-dependent behaviors of σ_{ac}, acting as insulators even at effective metal loads ranging from 7.0 to 9.5 wt%. This justifies the assumption that PA6 and Me-PA6 hybrids act as capacitors at the microstructural level. In theory, this effect can be attributed to the MWS polarization, which has been reported in both neat PA6 [14, 15] and PA6-metal hybrids obtained by AAROP [44].

For the hybrid plate with 5 wt% of CNT (Fig. 2c), the $\sigma(\omega)$ curve is very different, following the so-called universal dynamic response (UDR) given by [56, 57]:

$$\sigma(\omega) = \sigma_{dc} + \sigma_{ac} = \sigma_{dc} + A\omega^s \quad (5)$$

where σ_{ac} is the frequency-independent *dc* conductivity, A is a temperature-dependent parameter, and s is a temperature-dependent exponent ($0.5 < s < 1.0$). Expectedly, the s values should increase with decreasing temperature and increasing frequency [58].

The UDR concept defines that below a critical frequency, F_c, $\sigma(\omega)$ shows a frequency-independent plateau, whereas above F_c, a power-law dependence appears, i.e.:

$$\sigma(\omega) = \sigma_{ac} \propto \omega^s \quad (6)$$

The power law is recognized as an indicator of the translational motion of charges along the conductive network [31, 35, 59], which is formed by the nanosized CNT filler. In the case of CNT5 and all dually loaded samples of this study, it was considered that $\sigma(\omega) = \sigma_{dc}$ at $f = 0.1$ Hz [58]. Table 3 provides the values of σ_{dc}, F_c, and s extracted from the curves in Fig. 2c (CNT5) and Fig. 3a and b (all dually loaded metal-CNT plates) over the temperature range of 20–100 °C.

Notably, all samples containing CNT display power-law responses, which correspond remarkably well to the structural inhomogeneity of these samples, as demonstrated by the SEM images in Fig. 1. This observation also indicates that these samples contain an effective random resistor–capacitor (R–C) network,

Table 2 Temperature dependence of σ_{ac} for PA6 and monoload Me-PA6 containing composite plates

Sample	Real load (wt%)	T (°C)	σ_{ac} (S/cm) at f=0.1 Hz
PA6		20	4.77E−14
	–	50	7.33E−12
		100	3.01E−09
Al5		20	7.54E−12
	9.4	50	3.79E−10
		100	2.08E−08
Cu5		20	2.24E−12
	9.6	50	3.90E−10
		100	2.37E−08
Fe5		20	2.88E−12
	7.0	50	2.84E−10
		100	4.32E−08

Table 3 Parameters describing the electrical properties of the CNT5 and all dually loaded composite plates at different temperatures between 20 *and* 100 °C

Sample	T (°C)	σ_{dc} (S/cm) at f=0.1 Hz	F_c (Hz)	s
CNT5	20	9.97E−05	8.61E+04	0.63
	50	1.04E−04	5.34E+04	0.57
	100	1.02E−04	1.80E+04	0.52
Al3-CNT7	20	6.61E−03	-	-
	50	9.90E−03	-	-
	100	1.63E−02	-	-
Al5-CNT5	20	7.14E−04	2.93E+05	0.13
	50	9.43E−04	2.88E+05	0.15
	100	1.28E−03	2.24E+05	0.23
Al7-CNT3	20	1.42E−05	1.13E+04	0.41
	50	1.38E−05	5.64E+03	0.41
	100	1.21E−05	1.92E+03	0.43
Cu5-CNT5	20	2.78E−03	2.79E+05	0.11
	50	2.76E−03	2.79E+05	0.11
	100	3.71E−03	1.94E+05	0.17
Fe5-CNT5	20	4.04E−04	5.71E+04	0.28
	50	4.31E−04	5.48E+04	0.29
	100	4.08E−04	2.54E+04	0.30

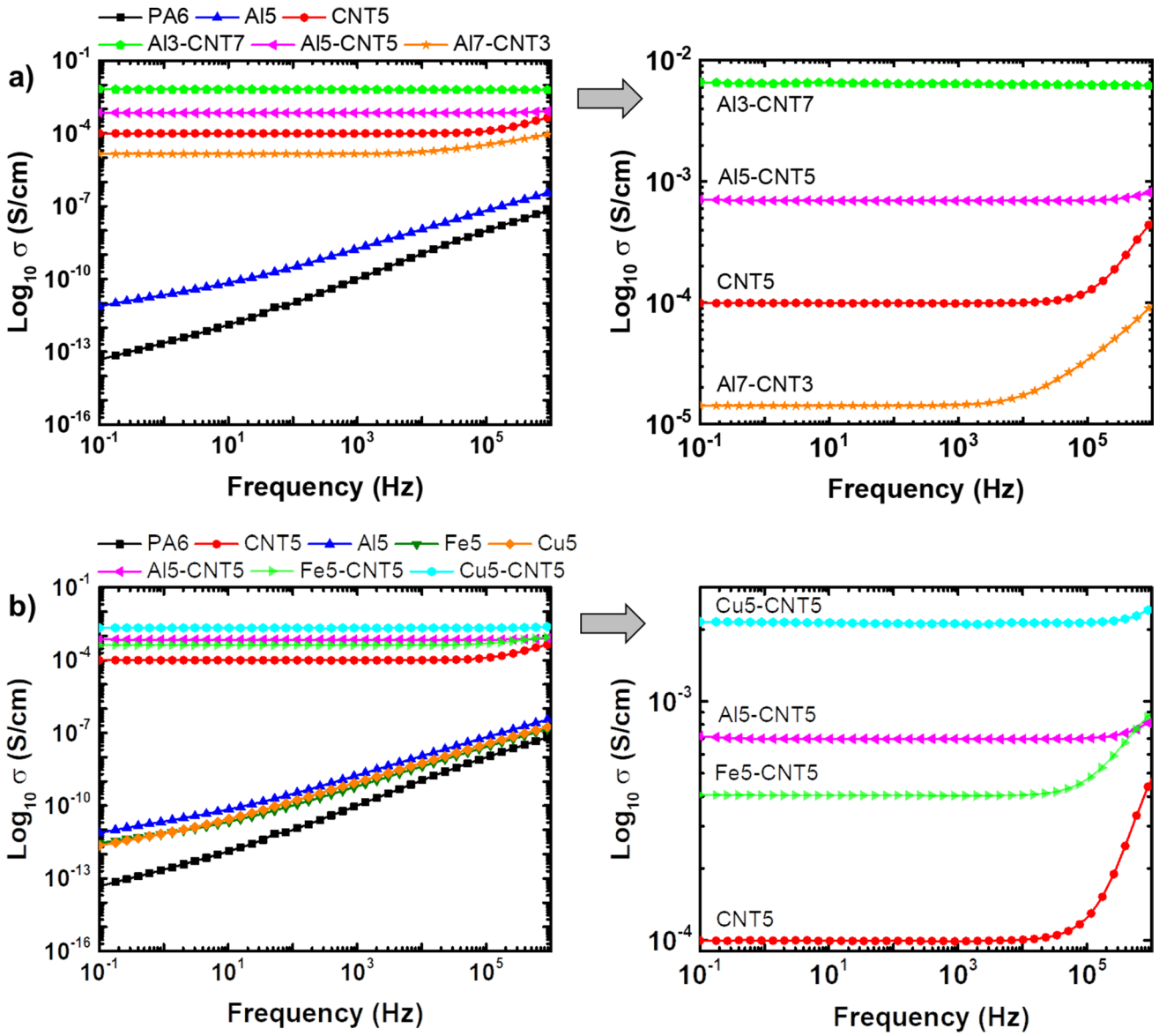

Figure 3 Electrical conductivity as a function of frequency at 20 °C of **a** Al-CNT composites and **b** metal-CNT 5/5 wt% composites. In both plots, composite plates containing 5 wt% of filler (either metal or CNT) are included for comparison. The plots on the right provide the respective magnified views of **a** and **b** for the most conductive composites.

consisting of conducting and dielectric insulating islands, respectively [53].

In the case of the PA6/Al-CNT composites (Fig. 3a and Table 2), it is evident that the electrical conductivity of the samples is predominantly influenced by the CNT content, while the sample containing only Al is an insulator. The σ_{dc} of CNT5 is 9.8×10^{-5} S/cm, which is lower than that of Al5-CNT5 binary hybrid with a $\sigma_{dc} = 8.1 \times 10^{-4}$ S/cm. This indicates a synergetic effect arising from the presence of Al microparticles within the CNT random conducting network. Therefore, incorporating more CNT in the Al3-CNT7 sample raises the conductivity to 6.6×10^{-3} S/cm, while conversely, reducing it in the Al7-CNT3 sample below that of the CNT5 sample. It seems that the charge transport within the dually filled composites predominantly relies on the nanosized CNT filler, which is enhanced by Al. Considering that the electrical conductivity for neat, 100 wt% CNT and Al metal components fall within the range of $0.5–2.0 \times 10^2$ S/cm and above 10^5 S/cm, respectively, it can be inferred that the significantly lower conductivity values observed

in the Al-CNT polyamide hybrids result from charge transport through a percolating network [31, 35]. The concentration, size, shape, and distribution of the filler particles within the matrix will be important factors in this case. Other studies have shown a similar effect involving different types of CNT- or graphene-containing composite materials [50, 60–64]. Figure 3a also demonstrates that at 20 °C, F_c falls below 10^6 Hz for CNT5, Al7-CNT3, and Al5-CNT5 samples. Conversely, in the Al3-CNT7 sample with the highest CNT amount, the electrical conductivity remains constant across the entire frequency range, indicating that F_c value has shifted above 1 MHz.

Figure 3b displays the electrical conductivity of metal-CNT 5/5 wt% composites at 20 °C, and the numeric data extracted from these curves within the 20–100 °C range are summarized in Table 2. Once more, it is observed that CNT determines the electrical conductivity of the binary composites, as the composites containing Fe and Cu particles behave as insulators like the neat matrix and Al5 samples (Fig. 3b and Table 2). Moreover, metals such as Cu and Fe also display a synergetic effect on electric conductivity when combined with CNT. The Cu metal particles, with volume content three times lower than that of Al, result in higher conductivities in the Cu5-CNT5 composite compared to the Al5-CNT5 sample. On the other hand, for the Fe5-CNT5 composite with a similar volume fraction of metal, the electrical conductivity values are lower than those of the Al5-CNT5 system.

The explanation of these observations can be related primarily to the specific electrical conductivity of the different metals. Specifically, the electric conductivity of Cu is about 6 times higher than that of Fe [62], which accounts for the differences in electrical conductivities of the respective binary composites. Furthermore, the morphology of the metal particles may have also played a role in influencing the conductivity. For instance, the Cu dendritic particles have sizes of ca. 20 µm [47], which could contribute to closer contact between the Cu particles and the CNT filler. In contrast, the spherical Fe particles have diameters of 3–5 µm [47], resulting in weaker contact with the CNT filler. Al particles were characterized as platelets [47], offering a larger surface area for interaction with the CNTs. This increased contact area likely facilitates enhanced electrical connectivity within the composite. Hence, the interaction between Al particles and CNTs may possess unique characteristics that enhance electrical conductivity. This interaction is believed to promote more efficient charge transfer between the components, thus justifying the observed synergistic effect within the CNT conducting network. This synergy is likely responsible for the improved connectivity and charge transport within the PA6 composites, resulting in enhanced electrical conductivity.

As mentioned above, both Fig. 3a and b illustrate that the electrical conductivity remains constant up to a certain F_c. Beyond the $F > F_c$, the conductive samples follow the power law $\sigma_{ac} \propto F^s$. The F^s characterizes the transport behavior in disordered materials and describes the frequency-dependent response of electrical conductivity [59], in this case for the conductive composites. Subsequently, at a certain F, there is a positive deflection of the conductive curve that can be attributed to the presence of charge carriers with different permittivities and conductivities (MWS relaxation) at the interfaces between different phases [50], which are PA6, CNT, and metal.

Figure 3 shows that σ_{dc} and F_c exhibit two instances of increase: (i) As the CNT content increases in the Al-CNT system (Fig. 3a), such that for the Al3-CNT7 sample, the σ_{dc} plateau extends across the entire frequency range, and (ii) as the electrical conductivity of the pure metal particles increases in the metal-CNT 5/5 wt% system (Fig. 3b). This behavior can be attributed to the formation of a conductive network that relies on both the CNT content and the electrical conductivity of the pure metal particles. Figure 4 represents this trend, incorporating data obtained at different temperatures as indicated in Table 2.

The s-exponent values (Table 2) for the CNT5 sample fall within the range of 0.52–0.63, aligning precisely with the UDR theory. With increasing temperatures above the T_g of ca. 50 °C, the s values decrease, indicating that higher temperatures enhance the mobility of charges through the conductive network. For samples with dual loading, the s values are lower than expected, ranging from 0.11 (Cu5-CNT5) to 0.41 (Al7-CNT3), where lower s-exponents correspond to higher conductivities. This discrepancy may be attributed to the fact that these samples exhibit relatively high electrical conductivity, causing the s exponent to not fully represent its true value within the measured frequency range. In these samples with dual loading, the s exponent is primarily associated with the initial part of the positive deflection in the conductivity curve. Nevertheless, the s values of the metal-CNT composites once again underscore the synergistic effect between CNT and metal particles

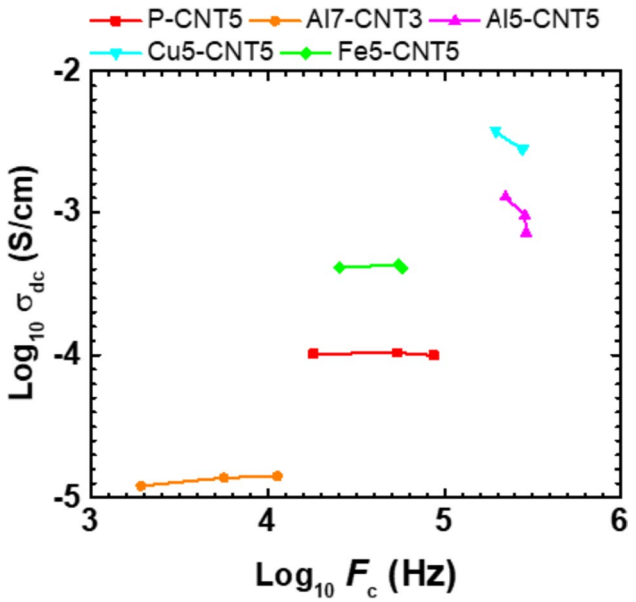

Figure 4 Electrical conductivity as a function of critical frequency for PA6-based composites at 20, 50, and 100 °C.

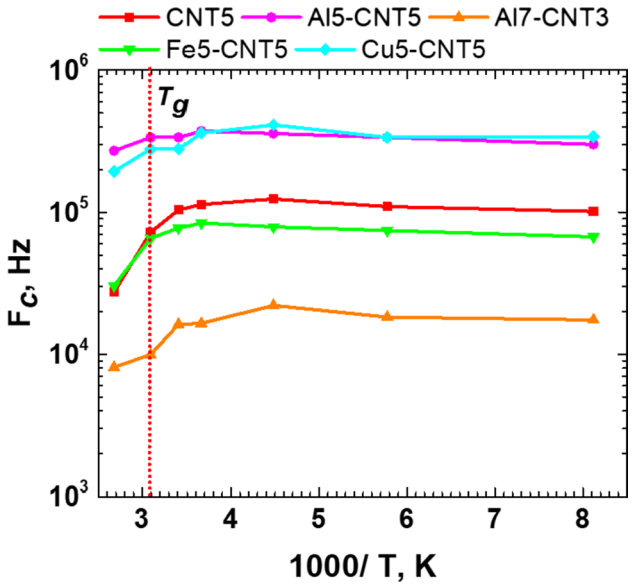

Figure 5 Critical frequency, F_c, as a function of the reciprocal temperature for conductive composites. Selected temperatures: 100, 50, 20, 0, −50, −100, and −150 °C. The dashed line indicates the T_g of the neat PA6 matrix.

concerning conductivity. All composites with mixed loading have lower *s* values compared to the sample with single CNT loading.

The temperature dependence of F_c was also investigated. Figure 5 shows the F_c as a function of the reciprocal absolute temperature T for the conductive composites. As observed, the F_c values appear to be temperature independent for $T < T_g$. However, at temperatures near or exceeding T_g, there is a slight decrease in F_c.

This temperature-related effect is more evident in samples with lower F_c values, such as Al7-CNT3, Fe5-CNT5, and CNT5, while it is less pronounced in Al5-CNT5 and Cu5-CNT5 samples. These findings suggest that temperature affects the conductance of the percolating network in all the composites studied. It is worth noting that Fig. 5 does not include sample Al3-CNT7 as its F_c would exceed the upper limit of the studied frequency range, i.e., above 10^6 Hz.

As a final part of the BDS study, we investigated the temperature dependencies of σ_{dc} for all PA6-based composites with single metal and CNT loading, as well as dual loading of metal-CNT. In Fig. 6, σ_{dc} for these composites is presented as a function of the reciprocal of the absolute T at a selected frequency. Figure 6a indicates that the *insulating* plates of PA6 and metal samples exhibit a temperature-dependent behavior across the entire temperature range, from − 150 to 100 °C. This behavior involves an increase in σ_{dc} as the temperature rises above T_g of the neat PA6 matrix. This phenomenon can be attributed to the improved mobility of dipoles as the material is heated. Conversely, in the CNT5 and all dually loaded samples (*semiconductors*), the σ_{dc} remains nearly temperature independent at low temperatures and exhibits a temperature-activated character at higher temperatures. This type of electrical conductivity is characteristic of percolating networks with a fluctuation-induced tunneling conductance (FITC) mechanism that is temperature independent and is commonly observed in CNT-containing polymer-based composites [31, 50, 63].

As shown in Fig. 6b, the temperature dependence of these materials can vary, as indicated by the slope of the segments at high temperatures. The previous studies [64, 65] have demonstrated that at $T > T_g$, the temperature dependence of σ_{dc} can be influenced by morphological variations within the matrix polymer, resulting in either a positive temperature coefficient (PTC) or a negative temperature coefficient (NTC). The PTC and NTC effects are associated with an increase or decrease in the resistivity of the studied system, respectively. In the context of this study, the Al3-CNT7, Cu5-CNT5, and Al5-CNT5 samples exhibit a

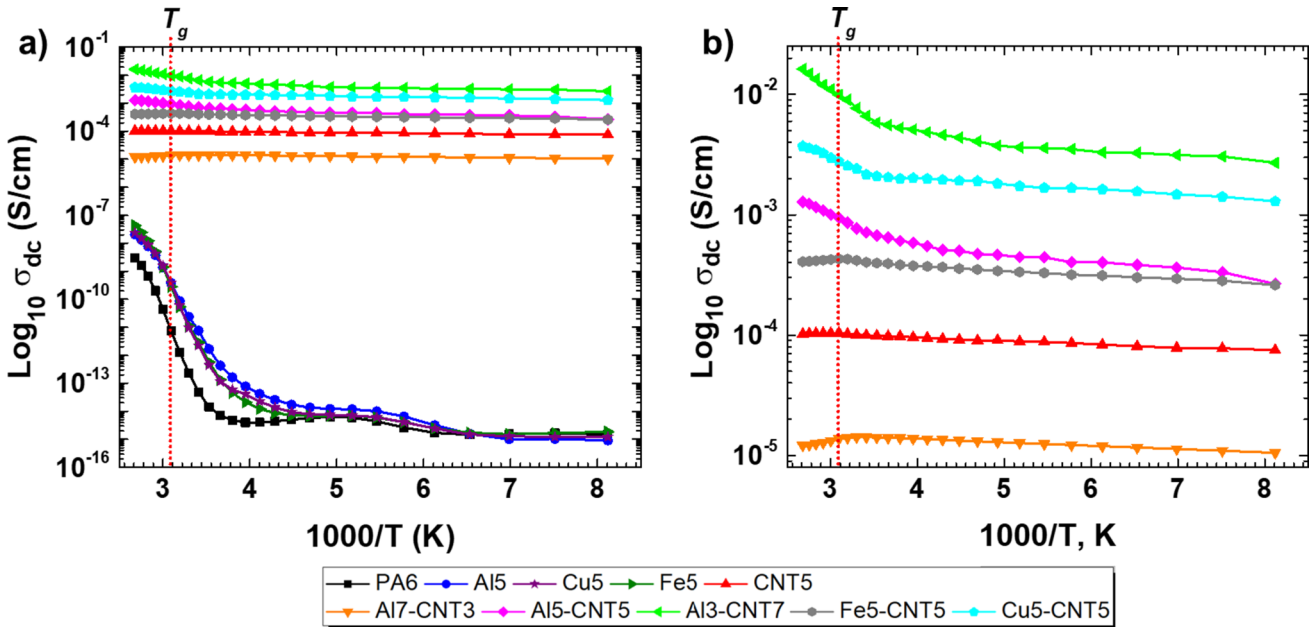

Figure 6 Electric conductivity, σ_{dc},, of the PA6-based composites as a function of the reciprocal temperature at $f = 0.1$ Hz: **a** mono- and dual-loaded composites and **b** magnification of **a** for dual-loaded composites. The dashed line represents the T_g of the neat PA6 matrix.

clear NTC effect, while the Al7-CNT3 and Fe5-CNT5 samples display the opposite PTC behavior. Interestingly, the CNT5 sample remains largely unaffected by temperature in the high-temperature segment of the curve above T_g.

Conclusions

The present study is the final publication of a series of papers investigating various aspects of the preparation, structural, and properties characterization of the mono- and dually reinforced PA6-based thermoplastic composites obtained via reactive microencapsulation strategy [43–47]. It represents a BDS study on the electrical conductivity of dually loaded PA6-based composite plates as a function of frequency and temperature. These thermoplastic composites, containing both metal (Me) and CNT, were obtained through sequential reactive encapsulation and compression molding. For comparative purposes, molded composites with only metals or CNT were also studied under the same conditions.

The results confirmed that the systems with metal monoloads remained electrical insulators across the entire range of temperatures and frequencies investigated. However, the same amount of CNT resulted in a semiconductor composite displaying a universal dynamic response, which is characteristic of the translational motions of charges within resistor–capacitor conducting networks. In the case of dually loaded metal-CNT composite plates, σ_{dc} increased by nine to eleven orders of magnitude at a temperature of 20 °C and a frequency of 0.1 Hz. This remarkable enhancement in electrical conductivity can be attributed to the coexistence of metal particles embedded within the CNT conducting network. Furthermore, this interaction also influenced the values of the critical frequency, F_c. The temperature dependence of the critical frequency, F_c, and σ_{dc} for all binary composite plates aligns with the fluctuation-induced tunneling conductance mechanism, which can be associated with a positive or negative temperature coefficient, depending on the type and concentration of the metal filler.

The present study demonstrates a remarkable increase in the electrical conductivity of PA6-based composites by incorporation of both metal microparticles and CNT into the thermoplastic matrix. This increase, driven by the synergistic interaction between CNT and metal particles, unveils promising prospects for structural and functional applications in industries such as automotive and electronics. These applications demand a rigorous control over electromagnetic interference shielding or dielectric behavior. Future

research will aim to enhance composite fabrication for industrial scalability and fine-tuning of loads within the PA6 matrix.

Acknowledgements

FMO and ZZD acknowledge the financial support by national funds through *Fundação para a Ciência e Tecnologia* (FCT), Project UID/CTM/50025/2019. FMO acknowledges also the FCT for the Ph.D. Grant PD/BD/114372/2016 (AdvaMTech Ph.D. Program in Advanced Materials and Processing). Part of this work has been also supported by Spanish MINECO through the Project MAT2015-66443-C02-1-R.

Author contributions

The manuscript was written through contributions of all authors. All authors have given approval to the final version of the manuscript.

Funding

Open access funding provided by FCT|FCCN (b-on).

Declarations

Conflict of interest All authors declare that there is no conflict of interest.

Supplementary Information The online version contains supplementary material available at https://doi.org/10.1007/s10853-023-09288-4.

References

[1] Fu X, Yao C, Yang G (2015) Recent advances in graphene/polyamide 6 composites: a review. RSC Adv 5:61688–61702. https://doi.org/10.1039/C5RA09312K

[2] Ghanta TS, Aparna S, Verma N, Purnima D (2020) Review on nano-and microfiller-based polyamide 6 hybrid composite: effect on mechanical properties and morphology. Polym Eng Sci 60:1717–1759. https://doi.org/10.1002/pen.25447

[3] Avakian P, Matheson RR, Starkweather HW (1991) Implications of dielectric response for the mechanism of changes in oxygen transport due to traces of moisture in amorphous nylons. Macromolecules 24:4698–4700. https://doi.org/10.1021/ma00016a033

[4] Noda N, Lee Y-H, Bur AJ et al (2005) Dielectric properties of nylon 6/clay nanocomposites from on-line process monitoring and off-line measurements. Polymer (Guildf) 46:7201–7217. https://doi.org/10.1016/j.polymer.2005.06.046

[5] Laredo E, Grimau M, Sánchez F, Bello A (2003) Water Absorption Effect on the Dynamic Properties of Nylon-6 by Dielectric Spectroscopy. Macromolecules 36:9840–9850. https://doi.org/10.1021/ma034954w

[6] Laurati M, Sotta P, Long DR et al (2012) Dynamics of water absorbed in polyamides. Macromolecules 45:1676–1687. https://doi.org/10.1021/ma202368x

[7] Füllbrandt M, Wellert S, von Klitzing R, Schönhals A (2015) Thermal and corrosion (in)stability of polyamide 6 studied by broadband dielectric spectroscopy. Polymer (Guildf) 75:34–43. https://doi.org/10.1016/j.polymer.2015.08.016

[8] Ryzhov VA (2022) Temperature evolution of the interaction of relaxation processes with local dynamics at terahertz frequencies in polymers with hydrogen bonds. Phys Solid State 64:124–128. https://doi.org/10.1134/S1063783422030040

[9] Černohorský P, Pisarenko T, Papež N et al (2021) Structure Tuning and Electrical Properties of Mixed PVDF and Nylon Nanofibers. Materials Basel 14:6096. https://doi.org/10.3390/ma14206096

[10] Avanesyan V, Salnikova Z (2020) Electric modulus spectroscopy of PA6/PA66 aliphatic polyamide. AIP Conf Proc 2308:30013. https://doi.org/10.1063/5.0035258

[11] Hammami I, Hammami H, Soulestin J et al (2019) Thermal and dielectric behavior of polyamide-6/clay nanocomposites. Mater Chem Phys 232:99–108. https://doi.org/10.1016/j.matchemphys.2019.04.048

[12] Tomara GN, Karahaliou PK, Anastassopoulos DL et al (2019) Effect of moisture and filler content on the structural, thermal and dielectric properties of polyamide-6/boehmite alumina nanocomposites. Polym Int 68:871–885. https://doi.org/10.1002/pi.5777

[13] Sanjeeva MN (2006) Hydrogen bonding, mobility, and structural transitions in aliphatic polyamides. J Polym Sci Part B Polym Phys 44:1763–1782. https://doi.org/10.1002/polb.20833

[14] Steeman PAM, Maurer FHJ (1992) Dielectric properties of polyamide-4,6. Polymer (Guildf) 33:4236–4241. https://doi.org/10.1016/0032-3861(92)90263-V

[15] Xu P, Zhang X (2011) Investigation of MWS polarization and dc conductivity in polyamide 610 using dielectric relaxation spectroscopy. Eur Polym J 47:1031–1038. https://doi.org/10.1016/j.eurpolymj.2011.02.016

[16] Atir S, Ali SH, Nimra SS et al (2023) Achieving enhanced EMI shielding with novel non-woven fabric using nylon fiber coated with polyaniline via in situ polymerization. Synth Met 293:117250. https://doi.org/10.1016/j.synthmet.2022.117250

[17] Zhou C, Zhu P, Wang Y et al (2023) Relaxation behavior, crystallization and mechanical property of long chain polyamides via thermodynamic technologies. Mater Today Commun 35:105568. https://doi.org/10.1016/j.mtcomm.2023.105568

[18] Li W, Chen M, Yang Y et al (2019) Dielectric property of modified barium titanate/polyamide 11 nanocomposites with different surfactants. J Appl Polym Sci 136:47447. https://doi.org/10.1002/app.47447

[19] Connor MT, Roy S, Ezquerra TA, Calleja FJB (1998) Broadband ac conductivity of conductor-polymer composites. Phys Rev B 57:2286–2294. https://doi.org/10.1103/PhysRevB.57.2286

[20] Lozano K, Bonilla-Rios J, Barrera EV (2001) A study on nanofiber-reinforced thermoplastic composites (II): Investigation of the mixing rheology and conduction properties. J Appl Polym Sci 80:1162–1172. https://doi.org/10.1002/app.1200

[21] Barrau S, Demont P, Peigney A et al (2003) DC and AC conductivity of carbon nanotubes−polyepoxy composites. Macromolecules 36:5187–5194. https://doi.org/10.1021/ma021263b

[22] Szymczyk A, Roslaniec Z, Zenker M et al (2011) Preparation and characterization of nanocomposites based on COOH functionalized multi-walled carbon nanotubes and on poly(trimethylene terephthalate). Express Polym Lett 5:977–995. https://doi.org/10.3144/expresspolymlett.2011.96

[23] Spitalsky Z, Tasis D, Papagelis K, Galiotis C (2010) Carbon nanotube–polymer composites: Chemistry, processing, mechanical and electrical properties. Prog Polym Sci 35:357–401. https://doi.org/10.1016/j.progpolymsci.2009.09.003

[24] Psarras GC, Manolakaki E, Tsangaris GM (2002) Electrical relaxations in polymeric particulate composites of epoxy resin and metal particles. Compos Part A Appl Sci Manuf 33:375–384. https://doi.org/10.1016/S1359-835X(01)00117-8

[25] Mamunya YP, Davydenko VV, Pissis P, Lebedev EV (2002) Electrical and thermal conductivity of polymers filled with metal powders. Eur Polym J 38:1887–1897. https://doi.org/10.1016/S0014-3057(02)00064-2

[26] Mazhar S, Qarni AA, Ul Haq Y et al (2020) Promising PVC/MXene based flexible thin film nanocomposites with excellent dielectric, thermal and mechanical properties. Ceram Int 46:12593–12605. https://doi.org/10.1016/j.ceramint.2020.02.023

[27] Cassignol C, Cavarero M, Boudet A, Ricard A (1999) Microstructure–conductivity relationship in conducting polypyrrole/epoxy composites. Polymer (Guildf) 40:1139–1151. https://doi.org/10.1016/S0032-3861(98)00349-8

[28] Bhattacharyya S, Saha SK, Mandal TK et al (2001) Multiple hopping conduction in interpenetrating polymer network composites of poly pyrrole and poly (styrene-co-butyl acrylate). J Appl Phys 89:5547–5551. https://doi.org/10.1063/1.1356435

[29] Moniruzzaman M, Winey KI (2006) Polymer Nanocomposites Containing Carbon Nanotubes. Macromolecules 39:5194–5205. https://doi.org/10.1021/ma060733p

[30] Hu N, Masuda Z, Yan C et al (2008) The electrical properties of polymer nanocomposites with carbon nanotube fillers. Nanotechnology 19:215701. https://doi.org/10.1088/0957-4484/19/21/215701

[31] Nogales A, Broza G, Roslaniec Z et al (2004) Low percolation threshold in nanocomposites based on oxidized single wall carbon nanotubes and poly(butylene terephthalate). Macromolecules 37:7669–7672. https://doi.org/10.1021/ma049440r

[32] Punetha VD, Rana S, Yoo HJ et al (2017) Functionalization of carbon nanomaterials for advanced polymer nanocomposites: a comparison study between CNT and graphene. Prog Polym Sci 67:1–47. https://doi.org/10.1016/j.progpolymsci.2016.12.010

[33] Abbasi H, Antunes M, Velasco JI (2019) Recent advances in carbon-based polymer nanocomposites for electromagnetic interference shielding. Prog Mater Sci 103:319–373. https://doi.org/10.1016/j.pmatsci.2019.02.003

[34] Zheng W, Wong S-C (2003) Electrical conductivity and dielectric properties of PMMA/expanded graphite composites. Compos Sci Technol 63:225–235. https://doi.org/10.1016/S0266-3538(02)00201-4

[35] Linares A, Canalda JC, Cagiao ME et al (2008) Broadband electrical conductivity of high density polyethylene nanocomposites with carbon nanoadditives: multiwall carbon nanotubes and carbon nanofibers. Macromolecules 41:7090–7097. https://doi.org/10.1021/ma801410j

[36] Paszkiewicz S, Szymczyk A, Špitalský Z et al (2012) Electrical conductivity of poly(ethylene terephthalate)/expanded graphite nanocomposites prepared by in situ polymerization. J Polym Sci Part B Polym Phys 50:1645–1652. https://doi.org/10.1002/polb.23176

[37] Sinitsin AN, Zuev VV (2016) Dielectric relaxation of fulleroid materials filled PA 6 composites and the study of its mechanical and tribological performance. Mater Chem Phys 176:152–160. https://doi.org/10.1016/j.matchemphys.2016.04.007

[38] Tamayo L, Palza H, Bejarano J, Zapata PA (2019) 8-Polymer composites with metal nanoparticles: synthesis, properties, and applications. In: Pielichowski K, Majka TM (eds) Polymer composites with functionalized nanoparticles. Elsevier, pp 249–286

[39] Wang Y, Lu S, He W et al (2022) Modeling and characterization of the electrical conductivity on metal nanoparticles/carbon nanotube/polymer composites. Sci Rep 12:10448. https://doi.org/10.1038/s41598-022-14596-x

[40] Yao S-S, Jin F-L, Rhee KY et al (2018) Recent advances in carbon-fiber-reinforced thermoplastic composites: A review. Compos Part B Eng 142:241–250. https://doi.org/10.1016/j.compositesb.2017.12.007

[41] Huang X, Jiang P (2015) Core-Shell Structured High-k Polymer Nanocomposites for Energy Storage and Dielectric Applications. Adv Mater 27:546–554. https://doi.org/10.1002/adma.201401310

[42] Denchev Z, Dencheva N (2014) Polyamide Microcapsules and Method to Produce the Same, patent application number PT107679, data filed: 03.06.2014 https://pt.espacenet.com/publicationDetails/originalDocument?CC=PT&NR=107679A&KC=A&FT=D&ND=3&date=20151203&DB=EPODOC&locale=pt_PT

[43] Dencheva N, Denchev Z, Lanceros-Méndez S, Ezquerra Sanz T (2016) One-step in situ synthesis of polyamide microcapsules with inorganic payload and their transformation into responsive thermoplastic composite materials. Macromol Mater Eng 301:119–124. https://doi.org/10.1002/mame.201500194

[44] Brêda C, Dencheva N, Lanceros-Mendez S, Denchev Z (2016) Preparation and properties of metal-containing polyamide hybrid composites via reactive microencapsulation. J Mater Sci 51:10534–10554. https://doi.org/10.1007/s10853-016-0274-0

[45] Oliveira F, Dencheva N, Martins P et al (2016) Reactive microencapsulation of carbon allotropes in polyamide shell-core structures and their transformation in hybrid composites with tailored electrical properties. Express Polym Lett 10:160–175. https://doi.org/10.3144/expresspolymlett.2016.15

[46] Oliveira F, Dencheva N, Lanceros-Méndez S et al (2019) Binary polyamide hybrid composites containing carbon allotropes and metal particles with radiofrequency shielding effect. Polym Compos 40:1338–1352. https://doi.org/10.1002/pc.24993

[47] Oliveira FM, Martins L, Dencheva NV et al (2022) Tunable electromagnetic interference shielding properties of binary thermoplastic composites prepared by reactive microencapsulation. ACS Appl Polym Mater 4:3482–3490. https://doi.org/10.1021/acsapm.2c00084

[48] Kremer F, Schönhals A (2003) Broadband dielectric spectroscopy, 1st edn. Springer, Berlin

[49] Shan G-F, Yang W, Yang M et al (2007) Effect of temperature and strain rate on the tensile deformation of polyamide 6. Polymer (Guildf) 48:2958–2968. https://doi.org/10.1016/j.polymer.2007.03.013

[50] Logakis E, Pandis C, Peoglos V et al (2009) Electrical/dielectric properties and conduction mechanism in melt processed polyamide/multi-walled carbon nanotubes composites. Polymer (Guildf) 50:5103–5111. https://doi.org/10.1016/j.polymer.2009.08.038

[51] Bowen CR, Almond DP (2006) Modelling the "universal" dielectric response in heterogeneous materials using microstructural electrical networks. Mater Sci Technol 22:719–724. https://doi.org/10.1179/174328406X101328

[52] Almond DP, Bowen CR (2004) Anomalous power law dispersions in ac conductivity and permittivity shown to be characteristics of microstructural electrical networks. Phys Rev Lett 92:157601. https://doi.org/10.1103/PhysRevLett.92.157601

[53] Almond DP, Vainas B (1999) The dielectric properties of random R–C networks as an explanation of the `universal' power law dielectric response of solids. J Phys Condens Matter 11:9081–9093. https://doi.org/10.1088/0953-8984/11/46/310

[54] Schönhals A, Kremer F (2003) Analysis of dielectric spectra. In: Kremer F, Schönhals A (eds) Broadband dielectric spectroscopy. Springer, Berlin, pp 59–98

[55] Vassilikou-Dova A, Kalogeras IM (2009) Dielectric analysis. In: Menczel JD, Prime RB (eds) Thermal analysis of polymers: fundametals and applications, 1st edn. Wiley, Hoboken, pp 497–614

[56] Jonscher AK (1977) The 'universal' dielectric response. Nature 267:673–679. https://doi.org/10.1038/267673a0

[57] Macdonald JR (2000) Comparison of the universal dynamic response power-law fitting model for conducting systems with superior alternative models. Solid State Ionics 133:79–97. https://doi.org/10.1016/S0167-2738(00)00737-2

[58] Kremer F, Różański SA (2003) The dielectric properties of semiconducting disordered materials. In: Kremer F, Schönhals A (eds) Broadband dielectric spectroscopy. Springer, Berlin, pp 475–494

[59] Dyre JC, Schroder TB (2000) Universality of ac conduction in disordered solids. Rev Mod Phys 72:873–892

[60] Valentini L, Bon SB, Lopez-Manchado MA et al (2016) Synergistic effect of graphene nanoplatelets and carbon black in multifunctional EPDM nanocomposites. Compos Sci Technol 128:123–130. https://doi.org/10.1016/j.compscitech.2016.03.024

[61] He L, Tjong S-C (2014) Electrical behavior and positive temperature coefficient effect of graphene/polyvinylidene fluoride composites containing silver nanowires. Nanoscale Res Lett 9:375. https://doi.org/10.1186/1556-276X-9-375

[62] Brandes EA, Brook GB (1992) General physical properties. In: Smithells metals reference book (7th edn). Butterworth-Heinemann, Oxford, pp 14–43

[63] Sheng P (1980) Fluctuation-induced tunneling conduction in disordered materials. Phys Rev B 21:2180–2195. https://doi.org/10.1103/PhysRevB.21.2180

[64] Meyer J (1973) Glass transition temperature as a guide to selection of polymers suitable for PTC materials. Polym Eng Sci 13:462–468. https://doi.org/10.1002/pen.760130611

[65] Zhang R, Tang P, Li J et al (2014) Study on filler content dependence of the onset of positive temperature coefficient (PTC) effect of electrical resistivity for UHMWPE/LDPE/CF composites based on their DC and AC electrical behaviors. Polymer (Guildf) 55:2103–2112. https://doi.org/10.1016/j.polymer.2014.02.065